

# Investigation on the Luminescence Properties of $\text{InMO}_4$ ( $M = \text{V}^{5+}$ , $\text{Nb}^{5+}$ , $\text{Ta}^{5+}$ ) Crystals Doped with $\text{Tb}^{3+}$ or $\text{Yb}^{3+}$ Rare Earth Ions

Pablo Botella,<sup>\*,†</sup> Francesco Enrichi,<sup>‡,‡</sup> Alberto Vomiero,<sup>‡,‡</sup> Juan E. Muñoz-Santiuste,<sup>§</sup> Alka B. Garg,<sup>||</sup> Ananthanarayanan Arvind,<sup>⊥</sup> Francisco J. Manjón,<sup>#</sup> Alfredo Segura,<sup>∇</sup> and Daniel Errandonea<sup>∇</sup>

<sup>†</sup>Department of Engineering Sciences and Mathematics, Luleå University of Technology, SE-97187 Luleå, Sweden

<sup>‡</sup>Department of Molecular Sciences and Nanosystems, Ca' Foscari University of Venice, via Torino 155, 30172 Venezia, Italy

<sup>§</sup>Departamento de Física, MALTA Consolider Team, Escuela Politécnica Superior, Universidad Carlos III de Madrid, Avenida de la Universidad 30, E-28913 Leganés, Spain

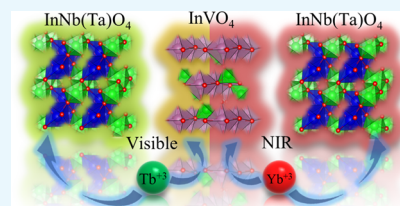
<sup>||</sup>High Pressure and Synchrotron Radiation Physics Division and <sup>⊥</sup>Process Development Division, Bhabha Atomic Research Centre, Mumbai 400085, India

<sup>#</sup>Instituto de Diseño para la Fabricación y Producción Automatizada, MALTA Consolider Team, Universitat Politècnica de València, Camí de Vera s/n, 46022 València, Spain

<sup>∇</sup>Departamento de Física Aplicada-ICMUV, Universidad de Valencia, MALTA Consolider Team, Edificio de Investigación, C. Dr. Moliner 50, 46100 Burjassot, Spain

## Supporting Information

**ABSTRACT:** We explore the potential of Tb- and Yb-doped  $\text{InVO}_4$ ,  $\text{InTaO}_4$ , and  $\text{InNbO}_4$  for applications as phosphors for light-emitting sources. Doping below 0.2% barely change the crystal structure and Raman spectrum but provide optical excitation and emission properties in the visible and near-infrared (NIR) spectral regions. From optical measurements, the energy of the first/second direct band gaps was determined to be 3.7/4.1 eV in  $\text{InVO}_4$ , 4.7/5.3 in  $\text{InNbO}_4$ , and 5.6/6.1 eV in  $\text{InTaO}_4$ . In the last two cases, these band gaps are larger than the fundamental band gap (being indirect gap materials), while for  $\text{InVO}_4$ , a direct band gap semiconductor, the fundamental band gap is at 3.7 eV. As a consequence, this material shows a strong self-activated photoluminescence centered at 2.2 eV. The other two materials have a weak self-activated signal at 2.2 and 2.9 eV. We provide an explanation for the origin of these signals taking into account the analysis of the polyhedral coordination around the pentavalent cations (V, Nb, and Ta). Finally, the characteristic green ( $^5\text{D}_4 \rightarrow ^7\text{F}_j$ ) and NIR ( $^2\text{F}_{5/2} \rightarrow ^2\text{F}_{7/2}$ ) emissions of  $\text{Tb}^{3+}$  and  $\text{Yb}^{3+}$  have been analyzed and explained.



## INTRODUCTION

Light-emitting diodes (LEDs) have attracted much attention in recent decades because of their properties of high brightness.<sup>1</sup> Lanthanide-doped oxides are suitable materials for these applications, particularly because of its robustness and flexibility for hosting different dopants.<sup>1</sup> Indium metal oxides with  $\text{InMO}_4$  ( $M = \text{V}^{5+}$ ,  $\text{Nb}^{5+}$ ,  $\text{Ta}^{5+}$ ) stoichiometry are included among them. These compounds are of interest not only because of its potential use as phosphors for LEDs<sup>2,3</sup> but also because of their ability to act as photocatalytic materials<sup>4–6</sup> and gas sensors.<sup>7,8</sup> All these applications are intimately related to the electronic band structure of the material. By modifying the electronic band structure, the optical and electronic properties of a given material can be tailored for specific applications. Several methods can be chosen to tune materials properties, such as high-pressure techniques,<sup>9–14</sup> ion irradiation,<sup>15,16</sup> and doping.<sup>2,3,17</sup> In particular, mechanical techniques modify material properties by deforming the lattice of the crystal. In contrast, chemical techniques, such as doping, modify the crystal structure very slightly for a doping below 1%, thus remaining the structure almost identical to the undoped sample.<sup>2,3,17</sup> However, the dopant, even in very small

proportions, introduces localized electronic levels that have a significant impact on the electronic and optical properties. In this context, it has been demonstrated that doping  $\text{InMO}_4$  ( $M = \text{V}^{5+}$ ,  $\text{Nb}^{5+}$ ,  $\text{Ta}^{5+}$ ) materials improves their performance as photocatalysts.<sup>18–22</sup> Moreover, they have also shown to be good host materials for rare earth (RE) ions, being the luminescence properties useful for LEDs.<sup>2,3,23,24</sup>

The crystal structures of indium niobate ( $\text{InNbO}_4$ ) and indium tantalate ( $\text{InTaO}_4$ ) are isomorphic and belong to the monoclinic space group  $P2_1/c$  of the wolframite structure (see Figure 1, left).<sup>9–11,25</sup> The structure has two formulae per unit cell ( $Z = 2$ );  $\text{Nb}(\text{Ta})^{5+}$  occupies the  $2e$  sites, while  $\text{In}^{3+}$  occupies the  $2f$  sites. Both  $\text{Nb}(\text{Ta})$  and  $\text{In}$  cations feature a 6-fold coordination. In fact, both  $\text{InO}_6$  and  $\text{Nb}(\text{Ta})\text{O}_6$  octahedral units are the building blocks of the structure because the crystal structure is constructed by edge- and corner-sharing of  $\text{InO}_6$  and  $\text{Nb}(\text{Ta})\text{O}_6$  zigzag chains parallel to the  $c$  direction and layered in the  $a$  direction.

Received: September 4, 2019

Accepted: December 16, 2019

Published: January 30, 2020

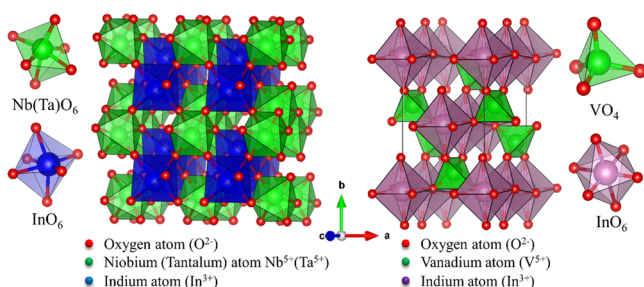


**Figure 1.** Crystal structure of the wolframite-type  $\text{InNb(Ta)O}_4$  host and coordination environments for  $\text{Nb}^{5+}(\text{Ta}^{5+})$  and  $\text{In}^{3+}$  (left) and orthorhombic  $\text{InVO}_4$  host and coordination environments for  $\text{V}^{5+}$  and  $\text{In}^{3+}$  (right) (for the color code of the structure, the reader is referred to the digital version).

Indium vanadate ( $\text{InVO}_4$ ) crystallizes in the orthorhombic space group  $Cmcm$  ( $Z = 4$ ) with  $\text{In}^{3+}$  and  $\text{V}^{5+}$  atoms occupying  $4a$  and  $4c$  sites, respectively.<sup>26,27</sup> The structure is composed of  $\text{InO}_6$  octahedral units and  $\text{VO}_4$  tetrahedral units as building blocks.  $\text{InO}_6$  octahedra are edge-sharing along the  $c$  axis, forming chains that are connected through  $\text{VO}_4$  tetrahedral units (see Figure 1, right). The octahedral units are more regular than the ones in the wolframite structures of the other compounds, and  $\text{VO}_4$  units are not linked between them.

It has been recently shown that  $\text{InVO}_4$ ,  $\text{InNbO}_4$ , and  $\text{InTaO}_4$  are wide band gap semiconductors.<sup>10</sup> These studies clarified the discrepancies reported in the literature about their band gap energy ( $E_g$ ) and about their band gap nature. Many of the controversies were due to a wrong assignment of the fundamental absorption edge to the absorption of light by defects.<sup>9,10</sup>  $\text{InVO}_4$  was shown to be a direct band gap semiconductor along the  $Y \rightarrow Y$  direction with an  $E_g$  of 3.62(5) eV, whereas  $\text{InNbO}_4$  and  $\text{InTaO}_4$  are indirect semiconductors along the  $Y \rightarrow \Gamma\text{-B}$  direction with  $E_g$  values of 3.63(5) and 3.79(5) eV, respectively. In all the compounds, states at the bottom of the conduction band (CB) are dominated by V 3d, Nb 4d, or Ta 5d, and O 2p states dominate the upper part of the valence band (VB).

Extensive experimental and theoretical works on doping  $\text{InVO}_4$ ,  $\text{InNbO}_4$ , and  $\text{InTaO}_4$  compounds by using nonmetal and metal elements have been reported.<sup>17–22</sup> However, regarding RE elements, mainly three of them ( $\text{Eu}^{3+}$ ,  $\text{Tm}^{3+}$ , and  $\text{Dy}^{3+}$ ) have been used for doping such compounds,<sup>2,3,23,24,28–31</sup> and only one work has been reported on Tb-doped  $\text{InTaO}_4$ .<sup>31</sup> Besides, it has been shown that  $\text{InVO}_4$ ,  $\text{InNbO}_4$ , and  $\text{InTaO}_4$  can be self-activated phosphors depending on the synthesis process, which can lead to modification of the morphology, pH, and M/In molar ratio and consequently of the luminescence properties.<sup>28,31–33</sup>

Here, we report a detailed study on the luminescence and optical properties of  $\text{InMO}_4$  ( $M = \text{V}^{5+}$ ,  $\text{Nb}^{5+}$ ,  $\text{Ta}^{5+}$ ) compounds by comparing undoped materials and materials doped with  $\text{Tb}^{3+}$  or  $\text{Yb}^{3+}$  RE ions. The self-activated luminescence of the undoped samples and the influence of the host lattice in the characteristic green and near-infrared (NIR) region emission lines of  $\text{Tb}^{3+}$  and  $\text{Yb}^{3+}$ , respectively, are also studied.

## RESULTS AND DISCUSSION

**Structural and Vibrational Analysis.** X-ray diffraction (XRD) patterns of all doped samples were collected in order to determine the crystal structure and purity and were compared

**Table 1.** Atomic % of the Dopants in  $\text{InVO}_4$ ,  $\text{InNbO}_4$ , and  $\text{InTaO}_4$  Compounds

dopant sample	$\text{Tb}^{3+}$	$\text{Yb}^{3+}$
$\text{InVO}_4$	0.19	0.17
$\text{InNbO}_4$	0.09	0.08
$\text{InTaO}_4$	0.07	0.15

to the XRD patterns of the undoped samples previously reported.<sup>9,11,12</sup> Table 2 and Figure 2 show the Rietveld refinement results and the XRD patterns (bars/columns under data represent the simulated XRD of undoped orthorhombic  $\text{InVO}_4$  and monoclinic  $\text{InNbO}_4$  and  $\text{InTaO}_4$ ), respectively. All diffraction peaks correspond to the orthorhombic  $\text{InVO}_4$  and wolframite  $\text{InNbO}_4$  and  $\text{InTaO}_4$  crystal structures. The host lattice was barely affected by the small concentration of the dopants used. Similar results have been also observed using other doping elements.<sup>2,3,17</sup> In these structures,  $\text{In}^{3+}$  has 6-fold octahedral coordination in all the samples, with an ionic radius of 0.8 Å. Considering the same valence and coordination,  $\text{Tb}^{3+}$  and  $\text{Yb}^{3+}$  have ionic radii of 0.923 and 0.868 Å, respectively. Therefore, RE ions can be assumed to occupy the  $\text{In}^{3+}$  sites in the  $\text{InVO}_4$ ,  $\text{InNbO}_4$ , and  $\text{InTaO}_4$  host lattices. Results from XRD and RS are consistent with this hypothesis. Only some residual material from precursors have been observed in the case of  $\text{InTaO}_4$  doped with  $\text{Yb}^{3+}$  (see Table 2). Even though RE ions possess bigger ionic radii than  $\text{In}^{3+}$ , it is observed that there is a small diminution of the lattice parameters leading to a reduction of the unit cell volume less than 1%, contrary to what would be expected (see Table 2). These variations of the lattice parameters could be ascribed to a distortion of the octahedral units when a foreign RE element is introduced into the crystal structure, which reduces the unit cell volume to accommodate the RE ions. As we will see later, these modifications will be reflected in the self-activated PL properties of the materials.

Raman measurements also support XRD observations. As can be seen in Figure 3, the Raman signal of the doped samples is similar to that of the previously reported undoped samples.<sup>9,11,12</sup> Although the dopants slightly modify the unit cell, no appreciable shifts or broadenings of the peaks were observed on the results. This is due to a small local disorder introduced in the crystalline network. Notice that if the dopants were located at interstitial sites, that is, not substituting indium, more important changes (likely with the appearance of new Raman modes) could have been found in the Raman spectrum. Therefore, Raman measurements support the claim that the RE atoms substitute In. Regarding the small changes in Raman frequencies, this can be related to the small unit cell volume change associated with doping. The reduction of the unit cell volume due to dopants can be seen as the effect of an external applied pressure to the material equivalent to 0.64, 1.14, and 0.7 GPa for  $\text{InVO}_4$ ,  $\text{InNbO}_4$  and  $\text{InTaO}_4$ , respectively.<sup>9–12</sup> These pressures would shift the Raman modes about 3–5  $\text{cm}^{-1}$ ; however, we have observed all the shifts to be lower than 2  $\text{cm}^{-1}$ , that is, within the instrumental resolution.

Thus, doping the sample with  $\text{Tb}^{3+}$  or  $\text{Yb}^{3+}$  does not modify appreciably the phonon frequencies of the compounds studied here. This also supports that RE are substituting the  $\text{In}^{3+}$  atoms, what excludes the possibility that they are placed in an interstitial position, which would, in principle, could give rise

**Table 2. Unit Cell Parameters and Goodness of the Rietveld Refinement for InVO<sub>4</sub>, InNbO<sub>4</sub>, and InTaO<sub>4</sub> Compounds and the Corresponding Doped Samples with Tb<sup>3+</sup> or Yb<sup>3+</sup> from our XRD Experiments and the Contribution of the Residual Precursor Materials Found on the InTaO<sub>4</sub>:Yb Sample**

sample	lattice parameters				$\Delta V$ (%)	goodness of the fit		
	<i>a</i> (Å)	<i>b</i> (Å)	<i>c</i> (Å)	$\beta$ (°)		<i>R<sub>p</sub></i>	<i>R<sub>wp</sub></i>	<i>R<sub>exp</sub></i>
InVO <sub>4</sub>	5.758	8.530	6.587			3.82	8.84	5.93
InVO <sub>4</sub> :Tb	5.747	8.506	6.563		−0.8	7.03	12.88	5.55
InVO <sub>4</sub> :Yb	5.744	8.501	6.565		−0.9	6.66	11.62	5.51
InNbO <sub>4</sub>	4.836	5.771	5.144	91.13		5.8	9.54	5.8
InNbO <sub>4</sub> :Tb	4.830	5.758	5.129	91.19	−0.6	4.93	8.1	4.32
InNbO <sub>4</sub> :Yb	4.832	5.760	5.129	91.17	−0.6	4.8	6.47	5.86
InTaO <sub>4</sub>	4.826	5.775	5.155	91.37		2.92	5.93	2.89
InTaO <sub>4</sub> :Tb	4.821	5.767	5.148	91.37	−0.4	4.01	5.82	5.18
InTaO <sub>4</sub> :Yb	4.823	5.767	5.149	91.35	−0.3	4.75	6.26	4.68
InTaO <sub>4</sub> :Yb contribution (%)		In <sub>2</sub> O <sub>3</sub>		Ta <sub>2</sub> O <sub>5</sub>		InTaO <sub>4</sub>		
		7.4		6.2		86.4		

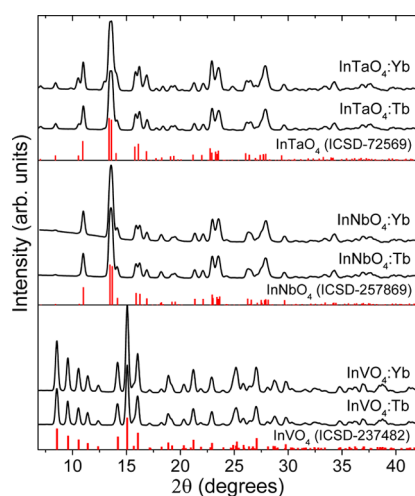


**Figure 2.** XRD patterns of InVO<sub>4</sub>, InNbO<sub>4</sub>, and InTaO<sub>4</sub> doped samples with Tb<sup>3+</sup> or Yb<sup>3+</sup>. Bars/columns data represent the standard ICSD charts of the undoped orthorhombic InVO<sub>4</sub> (ICSD-237482) and the undoped monoclinic InNbO<sub>4</sub> (ICSD-257869) and InTaO<sub>4</sub> (ICSD-72569), respectively. The height of the bars is proportional to the theoretical intensity of the peaks. Tables indicating the index, positions, and intensities of all reflections are included in the Supporting Information.

to local vibrational modes observable as RS peaks, such as those found in ZnO.<sup>41</sup>

**Optical and Photoluminescence Properties.** Optical reflectance and photoluminescence measurements of InVO<sub>4</sub>, InVO<sub>4</sub>:Tb, and InVO<sub>4</sub>:Yb samples are shown in Figure 4. The optical reflectance measurements for all samples are similar (see Figure 4, top), showing a broad asymmetric band feature from 2.8 to 4.6 eV with a maximum around 4.1 eV. For comparison, the calculated reflectance (*R*) has been also included. These data have been estimated using the calculated refractive index (*n*) by Mondal et al.<sup>42</sup> and using the Fresnel equation in the special case of normal incidence when the sample is immersed in air:

$$R = \left| \frac{n - 1}{n + 1} \right|^2 \quad (1)$$

The trend in the calculated reflectance is in good agreement with the observed spectra. However, due to the use of two different functionals, there is displacement of band gap energy

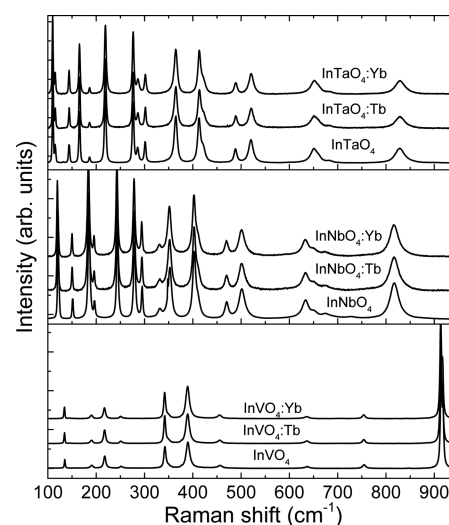


**Figure 3.** RS spectra of InVO<sub>4</sub>, InNbO<sub>4</sub>, and InTaO<sub>4</sub> compounds and the corresponding doped samples with Tb<sup>3+</sup> or Yb<sup>3+</sup>.

from 3.13 eV with density functional theory calculations to 4.02 eV with tight binding calculations.

The broad asymmetric reflectance band can be well described by two Gaussian functions peaking at 3.7 and 4.1 eV. According to Mondal et al.,<sup>42</sup> this energy region is due to the direct allowed interband transitions between the valence band and conduction band states caused by the charge transfer (CT) from O(p) to V(d) atoms inside the tetrahedral units. Thus, following previous results, we attribute these maximums to the two first direct optical allowed transition of InVO<sub>4</sub> at the Y → Y and Γ → Γ points of the Brillouin zone (BZ).<sup>10,27,42</sup> The first direct transition value is in very good agreement with the energy gap value determined from our optical absorption measurements (*E<sub>g</sub>* = 3.6 eV)<sup>10</sup> and consistent with the direct band gap nature. A reflectance maximum requires a strong optical absorption onset, which is the signature of an allowed direct transition. On the contrary, in indirect transitions, the optical transitions are very weak due to the need of phonon participation to conserve the momentum. Therefore, in direct gap semiconductors, the reflectance maximum and the fundamental absorption edge are expected at a similar energy. However, in indirect gap semiconductors, the first maximum of the reflectance corresponds to the first direct allowed transition, which is at a much higher energy than the indirect

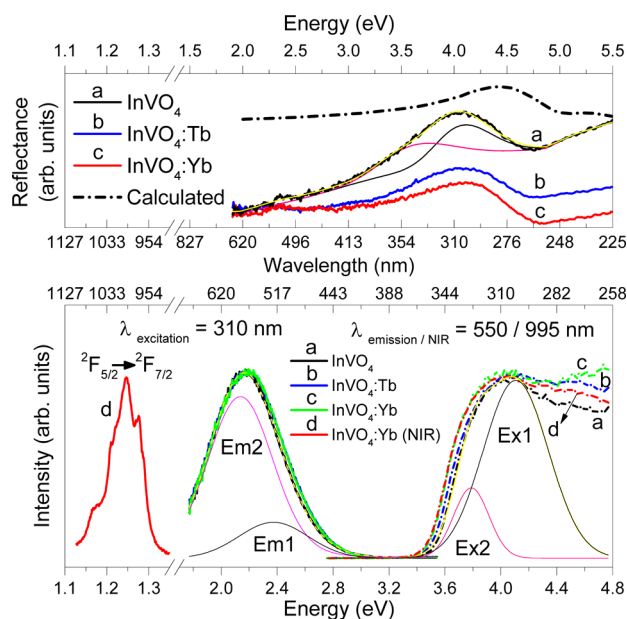


**Figure 4.** Optical reflectance (top) and PLE/PL spectra (bottom) of  $\text{InVO}_4$ ,  $\text{InVO}_4:\text{Tb}$ , and  $\text{InVO}_4:\text{Yb}$  (short dashed-dotted line corresponds to PLE data). The data were normalized for a better comparison of the emitted signals.

transition as it will be seen for the other two materials studied here.

The photoluminescence excitation (PLE) results are similar for all samples, showing a broad band starting at 3.4 eV and peaking around 4.1 eV (see Figure 4, bottom, short dashed-dotted line). For the PL signal, a very broad band similar for all the samples is seen peaking at 2.2 eV in the visible region (see Figure 4, bottom, solid line).  $\text{InVO}_4$  is a self-activated phosphor material due to the CT inside the vanadate group  $\text{VO}_4^{3-}$ . The vanadate oxoanion in a distorted tetrahedral coordination different from the ideal  $T_d$  symmetry where the transitions are spin-forbidden, presenting a self-activated luminescence due to the spin-orbit interaction that makes partly allowed the transitions.<sup>43–45</sup> In our case, the tetrahedral vanadate presents two different bond distances to the oxygen atoms, which makes the  $T_d$  symmetry degraded to the subgroup  $C_{2v}$ , giving rise to luminescence.

The PLE spectra show that the self-activated PL is excited by band to band transitions. These transitions were attributed to the direct transition from the ground state ( $^1A_1$ ) due to the oxygen 2p localized states to the excited Teltow (T) levels of the 3d vanadate states (see Figure 5, top). Due to the 3d metal character, the first excited level gives rise to four states, which, following the same nomenclature as in literature, are called  $^1T_1$ ,  $^1T_2$ ,  $^3T_1$ , and  $^3T_2$ , with a proposed level ordering as  $^3T_1 \approx ^3T_2 < ^1T_1 < ^1T_2$ .<sup>44</sup>

Following previous analysis,<sup>42–45</sup> the PLE spectra can be deconvoluted using two Gaussian functions as it can be seen in Figure 4, bottom. The Gaussian functions are peaking at 3.7 and 4.1 eV, which agree well to the direct transitions observed in the reflectance measurements. These energies are attributed to the direct transition from  $^1A_1$  to  $^1T_2$  (Ex1) and  $^1T_1$  (Ex2), respectively (see Figure 5, top). The PL spectra were also deconvoluted using two Gaussian functions peaking at 2.1 and 2.4 eV. These energy levels correspond to the radiative decay of  $^3T_2 \rightarrow ^1A_1$  (Em1) and  $^3T_1 \rightarrow ^1A_1$  (Em2) inside the  $\text{VO}_4^{3-}$  group.

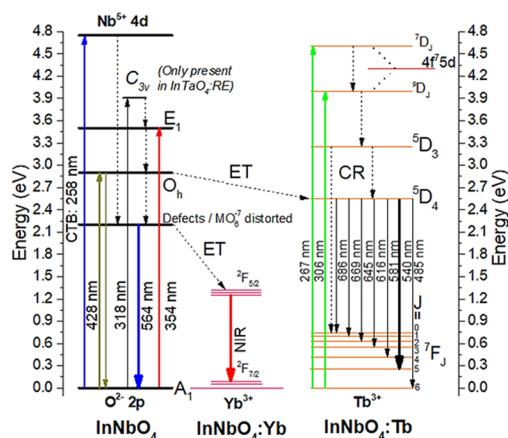
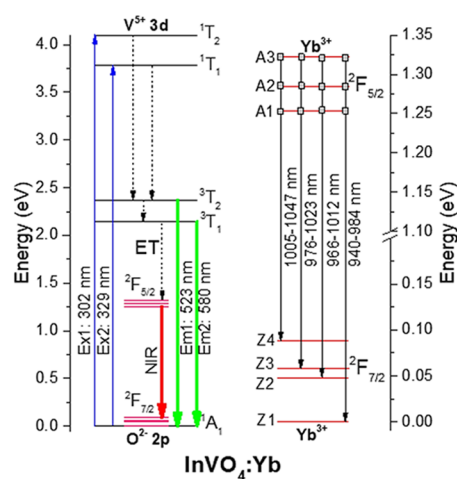


**Figure 5.** Energy level diagram of  $\text{InVO}_4$  doped with Yb (top) and  $\text{InNbO}_4$  doped with Yb or Tb (ET stands for electron transfer. CR stands for cross-relaxation. Dashed arrows represent nonradiative processes, and solid arrows correspond to PL emission and excitation).

In ref 46, a modest absorption in the visible light region above 2.5 eV was observed due to the existence of oxygen vacancies and defects in the  $\text{InVO}_4$  compound. However, they interpreted the observed luminescence as a consequence of these defects, forming a donor–acceptor pair that involves a deep donor state located at  $\sim 0.7$  eV below of the conduction band and an acceptor state that is located at  $\sim 0.3$  eV above the valence band. As it is discussed above and in ref 47, the luminescence is due to the CT inside the  $\text{VO}_4$  group and not to lattice defects or impurities as color centers. Instead, these defects or impurities play a role in the luminescence efficiency and exciton lifetime because they act as trap centers. Thus, the strong luminescence, a consequence of the distorted tetrahedral vanadate, could be affected by the presence of defects such as oxygen vacancies.

A small shift ( $< 0.1$  eV) can be observed in the PLE measurements, which could be attributed to the effect of the concentration and the distortion grade of the  $\text{VO}_4^{3-}$  groups, which affects the lattice parameters and influences the energy level positions of the excited states  $^1T_1$  and  $^1T_2$ .<sup>44</sup>

Only the self-activated PL emission from the host material was observed in the visible region, without any signal from the characteristic green emission lines of  $\text{Tb}^{3+}$ , which lay in the same spectral region (see Figure 5, bottom). However, in a

previous work,<sup>8</sup> it has been observed that there are characteristic  $\text{Eu}^{3+}$  lines even when  $\text{InVO}_4$  was doped with concentrations below to 2%. Different reasons have been suggested to the suppression of the emission lines of  $\text{Tb}^{3+}$  such as an inefficient energy transfer from the host material to the RE ions, a significant back-transfer rate, or a loss mechanism due to the  $\text{Tb}-\text{V}$  interaction via intervalence absorption.<sup>48,49</sup>

For the  $\text{InVO}_4:\text{Yb}$  sample, the PL signal was detected in the NIR (see Figure 4, bottom). We can attribute the PL signal in the NIR to the transitions from  ${}^2\text{F}_{5/2}$  to  ${}^2\text{F}_{7/2}$  energy levels of the  $\text{Yb}^{3+}$  atoms as it can be seen in the energy level diagram (see Figure 5, top) calculated in the way previously indicated using the structural data. Although the energy level scheme of  $\text{Yb}^{3+}$  is very simple and contains two multiplets, the  ${}^2\text{F}_{7/2}$  ground state and the  ${}^2\text{F}_{5/2}$  excited state, the electronic energy level scheme resulting from the simulation cannot be assumed as very accurate. This fact is related with the strong interaction of  $\text{Yb}^{3+}$  ions with the lattice vibration that usually gives rise to strong vibronic sidebands. In this case, the  $\text{Yb}^{3+}$  NIR luminescence consists of a broad band with small shoulders being difficult to identify the electronic transitions. Despite this uncertainty and to maintain the hypothesis that  $\text{Yb}^{3+}$  ions are actually substituting  $\text{In}^{3+}$  ions, we can attribute the PL signal in the NIR to the transitions from the  ${}^2\text{F}_{5/2}$  to  ${}^2\text{F}_{7/2}$  energy level of the  $\text{Yb}^{3+}$  atoms as it can be seen in the energy level diagram (see Figure 5, top). The proposed PL mechanism is as follows (see Figure 5, top): the UV photons are absorbed by the  $\text{VO}_4^{3-}$  groups in the host matrix (fundamental absorption from O 2p in the valence band to the V 3d levels in the conduction band generating an electron–hole pair), which transfer part of the energy to the  $\text{Yb}^{3+}$  ions by a nonradiative mechanism (the remaining energy is self-emitted), in which the electron–hole is captured by  $\text{Yb}^{3+}$  ions. The excited  $\text{Yb}^{3+}$  ions come back to the ground state through a radiative transition (due to the thermal motion, all  $A_n$  ( $n = 1, 2, 3$ ) levels are populated, and consequently, emissions from all of them are expected).<sup>50</sup>

Figure 6 shows the reflectance (top) and photoluminescence (bottom) spectra of  $\text{InNbO}_4$ ,  $\text{InNbO}_4:\text{Tb}$ , and  $\text{InNbO}_4:\text{Yb}$  samples. The calculated reflectance is also included, as estimated from the dielectric function calculated by Li et al.<sup>51</sup> and using eq 1 once the refractive index was calculated using the approximation  $n \approx \sqrt{\epsilon_1}$ , where  $\epsilon_1$  is the real part of the dielectric function. Despite the displacement due to the different functional used, the calculated reflectance describes well the experimental trend.

The optical reflectance spectra are similar for all the samples, showing two features around 4.7 and 5.3 eV. We identify these energies with the direct transitions from the VB to the CB at  $\Gamma \rightarrow \Gamma$  and  $Z \rightarrow Z$  points in the BZ, respectively.<sup>10</sup> These transitions yield different contributions to the dielectric function in different directions (anisotropic material), specifically for the  $xx$  component of the dielectric tensor, which show a shift to higher energies of the maximum with respect to  $yy$  and  $zz$  components.<sup>51</sup>

The PLE spectrum of undoped  $\text{InNbO}_4$ , in the measured range, shows a PLE peak with a maximum centered at 4.6 eV. This energy matches the direct transition observed by optical reflectance, and it is due to the charge transfer from the filled oxygen p states to the empty niobate d states inside of the octahedral unit  $\text{NbO}_4^{3-}$ .<sup>23,28</sup> However, due to the limitations of the PLE setup, we cannot observe the second maximum at a higher energy. From our previous work,<sup>10</sup> we know that  $\text{InNbO}_4$  is an indirect wide band gap semiconductor with the

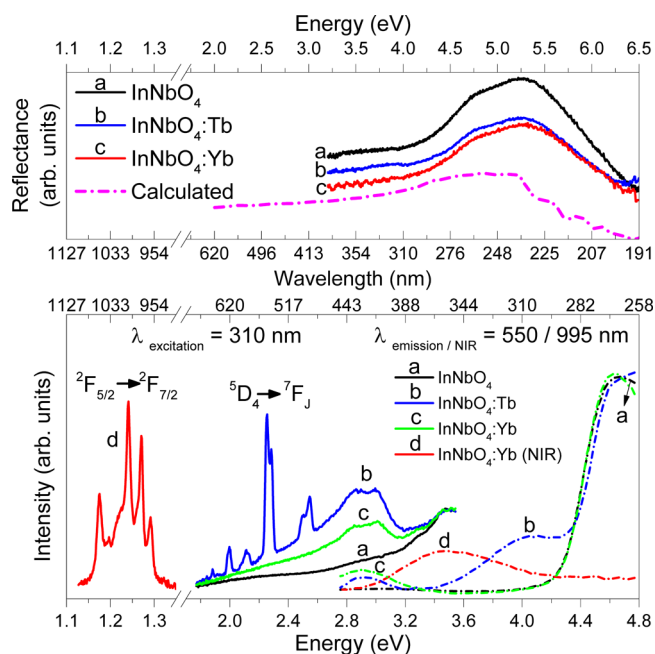


**Figure 6.** Optical reflectance (top) and PLE/PL spectra (bottom) of  $\text{InNbO}_4$ ,  $\text{InNbO}_4:\text{Tb}$ , and  $\text{InNbO}_4:\text{Yb}$  (short dashed-dotted line corresponds to PLE data). The data were normalized for a better comparison of the emitted signals.

valence band maximum (VBM) at the Y point and the conduction band minimum (CBM) in a point between the  $\Gamma$  and B direction of the BZ. Our optical absorption measurements yield an indirect energy gap value of 3.6 eV, which is smaller than the values found by PLE and optical reflectance. This is due to the indirect gap nature of the material as discussed previously.

For undoped  $\text{InNbO}_4$ , no fluorescence was found in the visible region (see Figure 6, bottom). Blasse et al.<sup>28</sup> reported similar results for undoped  $\text{InNbO}_4$  under UV radiation and only very weak blue emission at liquid nitrogen temperature. On the contrary, Feng et al.<sup>52</sup> found, in  $\text{InNbO}_4$  nanofibers and nanoparticles, a significant PL signal centered at 2.9 eV. This value well corresponds with the features found in the PLE results of the doped samples.

The PLE measurements of the doped samples exhibit several features apart from the fundamental absorption at 4.6 eV. In the case of  $\text{InNbO}_4:\text{Tb}$ , the fundamental absorption also lays at the same level as the  ${}^7\text{D}_J$  of the  $\text{Tb}^{3+}$  ions where most probably overlap both absorption bands (see Figure 5, bottom). In general, the excitation of  $\text{Tb}^{3+}$  in the UV spectral region may have different origins.<sup>53</sup> It can be attributed to the charge transfer (CT) from the orbitals 2p of  $\text{O}^{2-}$  to the 4f of  $\text{Tb}^{3+}$ <sup>54,55</sup> or to the spin-allowed transition between the  ${}^7\text{F}_6$  ground state and  ${}^7\text{D}_J$  ( $J = 1, 2, 3, 4, 5$ ) multiplets (low spin  $4f^75d$  excited states of  $\text{Tb}^{3+}$ ). Similarly, the feature around 4 eV may be related to the energy level  ${}^9\text{D}_J$  of the  $\text{Tb}^{3+}$  ion. This band is due to the spin-forbidden transition between the  ${}^7\text{F}_6$  ground state and  ${}^9\text{D}_J$  ( $J = 3, 4, 5, 6$ ) multiplets of the  $\text{Tb}^{3+}$  ion (high spin  $4f^75d$  excited states of  $\text{Tb}^{3+}$ ).<sup>56,57</sup> The feature at 2.9 eV, which also has been observed for the  $\text{InNbO}_4:\text{Yb}$  sample, could be related to impurity states (i.e., oxygen vacancies) introduced by the doping process or to a transition in the  $\text{NbO}_6^{7-}$  octahedral having an  $O_h$  symmetry that give rise to self-activated luminescence (i.e., the intrinsic luminescence of the material,

which does not originate from doping) in that region.<sup>52,58</sup> These distorted octahedral units, with lower symmetry than that of the ideal octahedron, could be the responsible for the decrease in the lattice parameter observed by XRD measurements.

In the case of  $\text{InNbO}_4\text{:Yb}$ , an additional band in the PLE spectrum is observed around 3.4 eV, which we called ( $E_1$ ) in the energy level diagram (see Figure S, bottom). This band only was observed by monitoring the emission in the NIR region; thus, this level transfers all the energy to the Yb atom that in turn radiatively decays emitting the characteristic NIR lines of the  $\text{Yb}^{3+}$  ions. This  $E_1$  level is related to the CT band of the 2p orbital of oxygen to 4f orbital of  $\text{Yb}^{3+}$  ions, which would directly populate the excited  $^2F_{5/2}$  level (see Figure S, bottom).<sup>59,60</sup>

The PL of the doped samples, besides the abovementioned feature around 2.9 eV, shows the characteristic green line emissions of  $\text{Tb}^{3+}$  atoms due to the  $^5D_4$  to  $^7F_J$  ( $J = 0, 1, 2, 3, 4, 5, 6$ ) transitions (see Figure S, bottom). In this case, the results obtained from the energy level simulation in highly satisfactory. Using the calculated  $^5D_4$  and  $^7F_J$  energy level positions, we can reproduce the position and width (due to the overlapping of the different transitions) of the observed emission bands. This fact strongly supports the hypothesis that  $\text{Tb}^{3+}$  are in substitutional configuration in the  $\text{InNbO}_4$  host matrix.

The  $^5D_4 \rightarrow ^7F_5$  transition always has the largest probability. This fact comes from the largest values of the reduced matrix elements both the electric dipole and the magnetic dipole ones for this transition.<sup>61</sup> We do not observe the  $^5D_3 \rightarrow ^7F_J$  luminescence, which is expected in the same spectral region around 2.9 eV. As commented previously, this feature is intrinsic of the material and not from the dopants. The  $^5D_3 \rightarrow ^7F_J$  luminescence is expected to be obtained when Tb excitation takes place at higher energies because the large  $^5D_3$ – $^5D_4$  energy separation (more than six lattice phonons) that makes the nonradiative  $^5D_3$ – $^5D_4$  relaxation highly unlikely.<sup>62</sup> The absence of this luminescence indicates that the ET channel (Figure S, bottom) from the host to the Tb ions does not take place at energies above 3.0 eV. Additionally, cross-relaxation mechanisms are often argued as the main  $^5D_3$ – $^5D_4$  depopulation channel in some other oxides with a similar Tb concentration.<sup>63,64</sup>

For the sample doped with  $\text{Yb}^{3+}$ , the characteristic NIR lines were observed at the same energy as in the  $\text{InVO}_4$  matrix but showing sharper emission peaks, suggesting a different interaction with the lattice and allowing a successful simulation from our crystal field calculation. Henderson and Imbusch showed that the electron–phonon coupling modifies the 4f electron wave-function description by introducing opposite-parity ones.<sup>62</sup> As a general result, the electron–phonon coupling takes part in many phenomena besides the vibronic sidebands, including shapes and widths of spectral lines and modification of the relaxation rates.<sup>64</sup> On this way, the different spectral shape obtained for the  $\text{InNbO}_4$  (and for  $\text{InTaO}_4$ , see further in the text) samples must be strongly related with the different (richest) phonon structures obtained in the Raman spectra for these samples.

Similar results are expected in the case of  $\text{InTaO}_4$  as it has the same crystal structure as  $\text{InNbO}_4$ . The reflectance (top) and photoluminescence (bottom) measurements of the  $\text{InTaO}_4$  undoped matrix and the doped samples are presented in Figure 7. As in  $\text{InNbO}_4$ , the reflectance spectra exhibit two

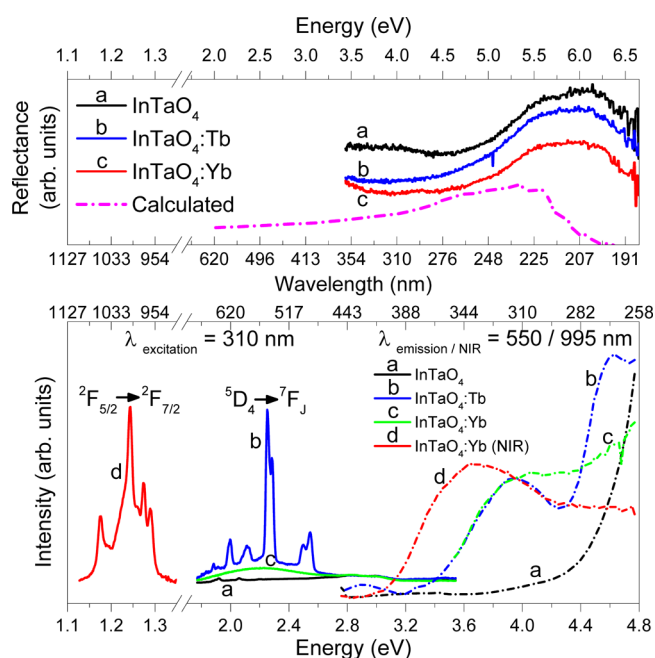


**Figure 7.** Optical reflectance (top) and PLE/PL spectra (bottom) of  $\text{InTaO}_4$ ,  $\text{InTaO}_4\text{:Tb}$ , and  $\text{InTaO}_4\text{:Yb}$  (short dashed-dotted line corresponds to PLE data). The data were normalized for a better comparison of the emitted signals.

features around 5.6 and 6.1 eV, which are associated with the direct transitions at the same points in the BZ as in  $\text{InNbO}_4$ , given the close similarity in the electronic band structure of both compounds.<sup>9,10</sup> The calculated reflectance was estimated in the same way as in the  $\text{InNbO}_4$ , showing that these maximums are an intrinsic feature of the dielectric function.

In the PLE measurement of the undoped sample, no maximum was observed due to the spectral range limitation.  $\text{InTaO}_4$  is a wider indirect band gap semiconductor (3.75 eV) by comparison to  $\text{InNbO}_4$ .<sup>9,10</sup> Thus, the direct transitions are expected to be at a higher energy than those in  $\text{InNbO}_4$ . This is because the distances of Ta–O in the  $\text{TaO}_6$  octahedra are smaller than those in the  $\text{NbO}_6$  octahedra, which makes the band gap wider.

In the PLE results of doped samples, basically, the same two features as in  $\text{InNbO}_4\text{:Tb}$  can be seen for  $\text{InTaO}_4\text{:Tb}$ . These features are due to  $\text{Tb}^{3+}$  ion absorption bands, and no contribution of the host in this case is possible due to the position of the fundamental absorption band at higher energies. However, an additional band can be seen around 3.9 eV, which gives rise to a broad band luminescence in the visible region. This band can be clearly seen for  $\text{InTaO}_4\text{:Yb}$  (see Figures 6 and 7 for comparison), and most probably, in the case of  $\text{InTaO}_4\text{:Tb}$ , this band overlaps with the self-absorption band of the  $\text{Tb}^{3+}$  ion at 3.9 eV. This signal was only observed for doped samples and again can be attributed to the defects introduced by the doping process or probably the formation of an additional distorted  $\text{TaO}_6^{7-}$  octahedral site with symmetry  $C_{3v}$ , as suggested by Chukova et al.<sup>58</sup>

Brixner et al.<sup>31</sup> reports that a properly prepared  $\text{InTaO}_4$  exhibits self-activated PL around 3 eV, and Zeng et al.<sup>33</sup> observed the PL signal for  $\text{InTaO}_4$  nanofibers and nanoparticles with a broad peak centered at 2.7 eV. In our measurements, the weak PL signal around 2.9 eV for  $\text{InTaO}_4$  (see Figure 7, bottom) is due to the same process as discussed

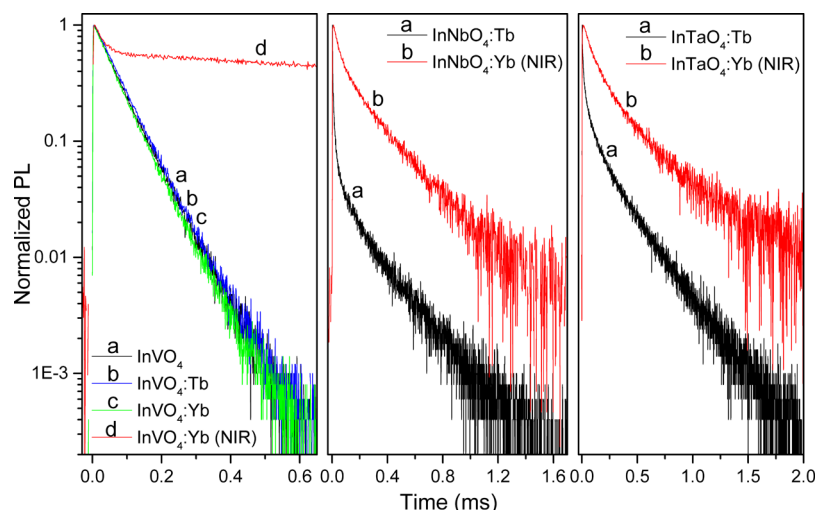


**Figure 8.** Time-resolved PL decay in the visible and NIR spectral regions for each matrix. The excitation wavelength was 310 nm, and emission wavelengths were 550 nm for visible and 995 nm for NIR.

for  $\text{InNbO}_4$ . A PL broad band from 1.7 to 2.6 eV is seen for  $\text{InTaO}_4$ :Yb in the visible region. This can be due to a self-activated PL of the host material associated with defects and vacancies, created by doping, as it is also present in the PL signal from  $\text{InTaO}_4$ :Tb. However, this emission is not observed in  $\text{InNbO}_4$  samples with  $O_h$  symmetry. Thus, most probably in the tantalate structure, there are octahedra with  $C_{3v}$  symmetry that generate this additional excited and emission level in the matrix.<sup>58</sup> Similar as in  $\text{InNbO}_4$ , the characteristic green emissions of  $\text{Tb}^{3+}$  atoms in the visible region are also observed in  $\text{InTaO}_4$ . About the NIR emissions of  $\text{Yb}^{3+}$ , it can be noticed that the emissions are stronger in  $\text{InNbO}_4$  than that in  $\text{InTaO}_4$  when normalized to the predominant emission at 2.24 eV.

Concerning time-resolved measurements, the decay curves and lifetimes of the characteristic emission lines of  $\text{Tb}^{3+}$  and  $\text{Yb}^{3+}$  and the self-activated  $\text{InVO}_4$  PL signal are shown in Figure 8 and Table 3, respectively. All the  $\text{RE}^{3+}$  emissions show

concentration is) followed by a long living tail (mainly associated with the pure radiative decay).

The decay time of the self-activated PL of  $\text{InVO}_4$  shows similar values even when it is doped by  $\text{RE}^{3+}$  ions, indicating that the decay time of the self-activated emission of  $(\text{VO}_4)^{3-}$  is not affected by doping. This behavior has been previously observed for  $\text{Sr}_3\text{La}(\text{VO}_4)_3$  when changing the doping concentration of  $\text{Eu}^{3+}$  (no variation of the decay time was observed), and the values agree with the values reported in the literature for the self-activated emission of the  $\text{VO}_4$  tetrahedral units embedded in different structures.<sup>43,66</sup> This implies that the electron transfer (ET) between  $(\text{VO}_4)^{3-}$  and  $\text{RE}^{3+}$  ions is not owing to the cross-relaxation between  ${}^3\text{T}_1$ ,  ${}^3\text{T}_2-{}^1\text{A}_1$  of  $(\text{VO}_4)^{3-}$  and  ${}^5\text{D}_4-{}^7\text{F}_1$  of  $\text{Tb}^{3+}$ , and the  ${}^2\text{F}_{5/2}-{}^2\text{F}_{7/2}$  of  $\text{Yb}^{3+}$ .<sup>43</sup>

The characteristic lifetime emission of the  $\text{Yb}^{3+}$  in the NIR region (997 nm) is, in general, long-lived (around 1 ms),<sup>67</sup> which is consistent with our measured decay time for  $\text{Yb}^{3+}$  ion in the  $\text{InVO}_4$  host. However, when  $\text{Yb}^{3+}$  is hosted in  $\text{InNbO}_4$  or  $\text{InTaO}_4$ , it shows similar values (0.2 ms) in both compounds due to the same environment of the RE ions in both isostructural compounds but with an unusual short decay time. Such a short lifetime could be attributed to the specific local environment or to a fast recombination such as defect states in these nanostructured materials. The short decay time could be a good feature for white LED application because it avoids saturation at a high excitation.<sup>68</sup> The lifetime of the characteristic emissions of  $\text{Tb}^{3+}$  in the visible region (550 nm) shows similar values in both  $\text{InNbO}_4$  and  $\text{InTaO}_4$  and is consistent with other compounds<sup>69</sup> due to the same environment of the RE as we commented previously for the case of  $\text{Yb}^{3+}$  ions. An interesting fact to explore in the future is the influence of the difference of maximum phonon energies in lifetime differences.<sup>9,11,12</sup>

Among the possible applications, these materials may be used as phosphors both in the visible and NIR spectral regions. In the visible region, an important parameter for the quality of the emitted color is given by the CIE chromatic coordinates. The calculated CIE ( $x$ ,  $y$ ) coordinates of  $\text{InVO}_4$ ,  $\text{InNbO}_4$ :Tb, and  $\text{InTaO}_4$ :Tb are shown in Figure 9, while Table 4 lists the CIE coordinates values, correlation color temperature (CCT), color rendering indices (CRI), and the color emitted from each sample. In  $\text{InVO}_4$ , as it is a self-activated phosphor, they are

**Table 3. Lifetime Values of the Characteristic Emission Lines of  $\text{Tb}^{3+}$ ,  $\text{Yb}^{3+}$ , and Self-Activated  $\text{InVO}_4$  Band**

sample	emission (nm)	B1	$\tau_1$ ( $\mu\text{s}$ )	B2	$\tau_2$ ( $\mu\text{s}$ )	$\tau_{\text{average}}$ ( $\mu\text{s}$ )
$\text{InVO}_4$	550					69
$\text{InVO}_4$ :Tb	550					71
$\text{InVO}_4$ :Yb	550					66
$\text{InVO}_4$ :Yb (NIR)	995	2500	25	2398	2334	1997
$\text{InNbO}_4$ :Tb	550	793	12	344	232	210
$\text{InNbO}_4$ :Yb (NIR)	997	2439	62	1659	340	249
$\text{InTaO}_4$ :Tb	550	2262	25	755	263	202
$\text{InTaO}_4$ :Yb (NIR)	999	2632	107	1325	461	241

double exponential decay, which is frequently observed when the excitation energy is transferred from the donor  $\text{MO}_4^{3-}$  ( $M = \text{V}, \text{Nb}, \text{Ta}$ ) to the activator ion  $\text{Tb}^{3+}$  or  $\text{Yb}^{3+}$  in this case.<sup>65</sup> In nonheavily doped samples, the characteristic behavior of the luminescence decays shows a typical initial fast decay (related with the transfer mechanism and faster as higher the

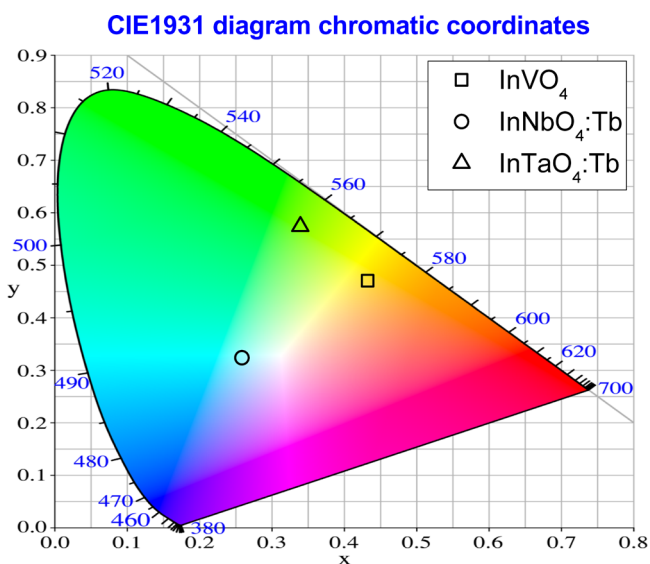


Figure 9. CIE diagram of  $\text{InVO}_4$ ,  $\text{InNbO}_4\text{:Tb}$ , and  $\text{InTaO}_4\text{:Tb}$ .

Table 4. Chromaticity Coordinates (CIE), Correlated Color Temperature (CCT), Color Rendering Indices (CRI), and Color Emitted for  $\text{InVO}_4$ ,  $\text{InNbO}_4\text{:Tb}$ , and  $\text{InTaO}_4\text{:Tb}$  Samples

sample	x	y	CCT (K)	CRI (%)	color
$\text{InVO}_4$	0.43	0.47	3561	71	between warm white and neutral white
$\text{InNbO}_4\text{:Tb}$	0.26	0.33	9895	37	overcast sky, slightly blue-green
$\text{InTaO}_4\text{:Tb}$	0.34	0.58	5379	27	between daylight and sunlight

only estimated for the undoped sample.  $\text{InVO}_4$ ,  $\text{InNbO}_4\text{:Tb}$ , and  $\text{InTaO}_4\text{:Tb}$  present yellowish-orange, green-yellow, and greenish-blue color code coordinates, respectively. Among them, self-activated  $\text{InVO}_4$  presents a good CRI of 71, which is already interesting for lighting applications. Furthermore, proper combination of the three phosphors may further improve the quality of the light emission; thus, they can be considered promising candidates for white LEDs or NIR emitting sources in the case of Yb-doped samples. The capability of converting UV photons in visible or NIR photons has also potential applications, improving the efficiency of silicon-based solar cells.

## CONCLUSIONS

Doping  $\text{InVO}_4$ ,  $\text{InNbO}_4$ , and  $\text{InTaO}_4$  with  $\text{Tb}^{3+}$  or  $\text{Yb}^{3+}$  up to 0.2% at. concentration does not change the crystal structure and phonon frequencies of the host materials but provides peculiar optical excitation and emission properties in the visible and NIR spectral regions. The energy of the two first direct transitions was estimated in  $\text{InVO}_4$  at 3.7/4.1 eV in the  $Y \rightarrow Y$  and  $\Gamma \rightarrow \Gamma$  points in the BZ and in  $\text{InNbO}_4$  and  $\text{InTaO}_4$  at 4.7/5.3 and 5.6/6.1 eV in the  $\Gamma \rightarrow \Gamma$  and  $Z \rightarrow Z$  points in the BZ, respectively.  $\text{InVO}_4$ , being a direct band gap semiconductor, showed a strong self-activated photoluminescence centered at 2.2 eV, in comparison with the indirect  $\text{InNbO}_4$  and  $\text{InTaO}_4$  semiconductors that showed weak self-activated signals at 2.2 and 2.9 eV. These signals were related to the irregular tetrahedral  $\text{VO}_4^{3-}$  in  $\text{InVO}_4$  and the octahedra

$\text{Nb}(\text{Ta})\text{O}_4^{3-}$  in  $\text{InNbO}_4$  and  $\text{InTaO}_4$ , respectively. The characteristic green ( $^5\text{D}_4 \rightarrow ^7\text{F}_j$ ) and NIR ( $^2\text{F}_{5/2} \rightarrow ^2\text{F}_{7/2}$ ) emission of  $\text{Tb}^{3+}$ - and  $\text{Yb}^{3+}$ -doped materials were analyzed, demonstrating to be potential candidates for applications as phosphors for white LED lighting and NIR emitting sources and improving the efficiency of silicon-based solar cells.

## EXPERIMENTAL SECTION

Undoped  $\text{InMO}_4$  ( $M = \text{V}^{5+}$ ,  $\text{Nb}^{5+}$ ,  $\text{Ta}^{5+}$ ) powders were prepared by a solid-state reaction following the method reported in previous works.<sup>9–12</sup> The composition and purity of the samples were confirmed by energy-dispersive X-ray spectroscopy analysis (EDAX) using a transmission electron microscope operated at 200 kV. The crystal structure was verified by powder (XRD) measurements and Raman spectroscopy (RS) measurements at room conditions, and the results were previously published.<sup>9,11,12</sup>

Polycrystalline  $\text{InMO}_4\text{:RE}$  ( $M = \text{V}^{5+}$ ,  $\text{Nb}^{5+}$ ,  $\text{Ta}^{5+}$ ;  $\text{RE} = \text{Tb}^{3+}$ ,  $\text{Yb}^{3+}$ ) doped samples having  $\text{Tb}^{3+}$  or  $\text{Yb}^{3+}$  concentrations below 0.2% (see Table 1) were synthesized with the solid-state reaction method using predried powders of  $\text{In}_2\text{O}_3$ ,  $\text{Nb}_2\text{O}_5$ ,  $\text{Ta}_2\text{O}_5$ ,  $\text{V}_2\text{O}_5$ ,  $\text{Yb}_2\text{O}_3$ , and  $\text{Tb}_4\text{O}_7$  (purity of >99.9%). The low doping concentration was selected following a previous work on Eu-doped  $\text{InVO}_4$  with the aim of obtaining good luminescence properties without affecting the crystal structure of the host material. For the doped tantalate and niobate, respective binary oxides were weighed in a stoichiometric ratio, thoroughly ground in a pestle and mortar, compacted by cold pressing into cylinders of 12.5 mm in diameter and 5 mm in height, and fired at 1100 °C for 24 h in a box-type resistive furnace followed by another heat treatment at 1200 °C for 24 h. For the vanadate, the first heating was carried out at 700 °C for 24 h followed by second heat treatment at 850 °C. All the samples are in a powder form.

Compositions were confirmed by EDS. The EDS measurements were performed using an Oxford Instruments X Max 80 EDS system attached to a Philips XL30ESEM. During EDS measurements, an accelerating voltage of 30 kV was employed. Since the samples are nonconducting, the ESEM was operated in environmental mode, where surface charge buildup on the sample was neutralized using water vapor. The accuracy of the EDS measurements was ensured by measurements of standard samples of known compositions in environmental mode. Each determination is the average of 32 runs, and at least three places were analyzed on each sample.

The crystal structures, as well as the possible structural modification introduced by the dopants, have been studied by XRD and RS techniques. For XRD measurements, a laboratory-based powder XRD using a rotating-anode generator (RAG) with a Mo ( $\lambda = 0.7107 \text{ \AA}$ ) anode and a MAR345 area detector was used. RS measurements were excited with the 632.8 nm line of a He-Ne gas laser using a power of 2 mW. The scattered light was collected through a 50 $\times$ /0.35 objective and sent to a Horiba Jobin Yvon LabRAM HR spectrometer with an edge filter cutting Raman signals below  $\sim 50 \text{ cm}^{-1}$ . The signal was dispersed by a grating of 1200 grooves/mm and detected by a thermoelectrically cooled multichannel charge-coupled device detector enabling a spectral resolution below  $2 \text{ cm}^{-1}$ .

For optical reflectance measurements in the UV–Vis–NIR at normal incidence, an optical setup consisting of a deuterium lamp, fused silica lenses, reflecting optics objectives, and a UV–Vis spectrometer was used.<sup>34</sup>

Photoluminescence excitation (PLE) and emission (PL) spectra were recorded by an Edinburgh Instruments FLS980 photoluminescence spectrometer. A continuous-wave xenon lamp was used as an excitation source for steady-state measurements, coupled to a double-grating monochromator for wavelength selection. The light emitted from the sample was collected by a double-grating monochromator and recorded by a photon counting R928P photomultiplier tube cooled at  $-20\text{ }^{\circ}\text{C}$  in the visible spectral region and a R5509-73 photomultiplier tube cooled at  $-80\text{ }^{\circ}\text{C}$  in the NIR spectral region.

The PLE signal was measured by following the emission signal at 550 nm (2.25 eV) and in the case of samples doped with  $\text{Yb}^{3+}$  also at 995 nm (1.25 eV). PL emission was measured in the visible region and in the case of samples doped with  $\text{Yb}^{3+}$  and also in the NIR region by using 310 nm (4 eV) excitation.

Time-resolved PL emission was obtained in multichannel scaling (MCS) mode, exciting the sample by a microsecond xenon flash lamp with a pulse duration of 1–2  $\mu\text{s}$  and a repetition frequency of 10 Hz by using the same PMT detectors described above. The decay time was measured for the same signals as in PLE measurements. All abovementioned measurements were carried out at room temperature.

**Computational Methods.** The energy level scheme of  $\text{Tb}^{3+}$  and  $\text{Yb}^{3+}$  ions inside the crystals was modeled using a parametrized one-electron Hamiltonian in the  $4f^n$  ground configuration. The usual description includes both the several superimposed atomic interactions, which generate the  $^{2S+1}L_J$  multiplets, and the effect of the crystal field felt by the shielded 4f shell electron, when a rare earth ion incorporates into a solid host. The crystal field reflects the local symmetry of the RE location and is responsible for the breaking down of the  $^{2S+1}L_J$  degeneracy giving rise to the Stark levels. The total Hamiltonian can be expressed as<sup>35</sup>

$$\begin{aligned}
 H = E_{\text{AVE}} + \sum_{k=2,4,6} F^{(k)} \cdot f_k + \zeta_{4f} \sum_{i=1}^N s_i \cdot l_i + \alpha \cdot L^2 \\
 + \beta \cdot G(G_2) + \gamma \cdot G(R_2) + \sum_{r=2,3,4,6,7,8} T^{(r)} \cdot t_r \\
 + \sum_{j=0,2,4} M^{(j)} \cdot m_j + \sum_{k=2,4,6} P^{(k)} \cdot p_k + \sum_{k=2,4,6} B_0^k \cdot C_0^{(k)} \\
 + \sum_{q>0}^{\leq k} [B_q^k \cdot (C_{-q}^{(k)} + (-1)^q C_q^{(k)}) \\
 + iB_q^k \cdot (C_{-q}^{(k)} + (-1)^q C_q^{(k)})] \quad (2)
 \end{aligned}$$

Most of the parameters in the atomic Hamiltonian ( $E_{\text{AVE}}$ ,  $F^{(k)}$ ,  $\zeta_{4f}$ ,  $\alpha$ ,  $\beta$ ,  $\gamma$ ,  $M^{(j)}$ ,  $P^{(k)}$ , and  $T^{(r)}$ ) were fixed to previously reported values in the present calculation.<sup>35–37</sup> Only  $E_{\text{AVE}}$ , the Slater  $F^2$  parameter (for  $\text{Tb}^{3+}$ ), and the spin–orbit  $\zeta_{4f}$  parameter are slightly varied to properly estimate the position and separation of the multiplets involved in the observed transitions.

The number of nonvanishing parameters in the crystal field Hamiltonian depends on the point symmetry of the rare earth site in the host. For the studied structures, and due to the similarity of their ionic radius, we can assume that the  $\text{RE}^{3+}$  ion replaces the  $\text{In}^{3+}$  ions in sites with  $D_2$  local symmetry for  $\text{InMO}_4$  ( $M = \text{Ta}, \text{Nb}$ ) compounds or  $C_{2h}$  local symmetry for  $\text{InVO}_4$  crystals. In these symmetries, the degeneracies of the

$^{2S+1}L_J$  multiplets are completely lifted. By appropriated selection of the crystal field quantization axis, and a subsequent suitable rotation around the  $z$  axis to get  $B_2^2 = 0$ , both symmetries can be described by a crystal field Hamiltonian having only 14 nonvanishing parameters. The crystal field Hamiltonian takes the form

$$\begin{aligned}
 H_{\text{CF}} = B_0^2 C_0^2 + B_2^2 (C_{-2}^2 + C_2^2) + B_0^4 C_0^4 \\
 + B_2^4 (C_{-2}^4 + C_2^4) + iB_2^4 (C_{-2}^4 + C_2^4) \\
 + B_4^4 (C_{-4}^4 + C_4^4) + iB_4^4 (C_{-4}^4 + C_4^4) \\
 + B_0^6 C_0^6 + B_2^6 (C_{-2}^6 + C_2^6) + iB_2^6 (C_{-2}^6 + C_2^6) \\
 + B_4^6 (C_{-4}^6 + C_4^6) + iB_4^6 (C_{-4}^6 + C_4^6) \\
 + B_6^6 (C_{-6}^6 + C_6^6) + iB_6^6 (C_{-6}^6 + C_6^6) \quad (3)
 \end{aligned}$$

The CF parameters were calculated using a modified version of the simple overlap model (SOM)<sup>38</sup> that correlates the bond distance and the bond valence as in the usual bond valence model (details can be obtained from refs 14 and 39). The crystallographic positions of the  $\text{In}^{3+}$  ion and its oxygen ligands obtained by ab initio calculations for every host matrix were used neglecting the small distortion of the  $\text{In}^{3+}$  site when occupied by a  $\text{RE}^{3+}$  ion. Following standard convention in the description of the crystal field interaction, the rotationally invariant crystal field strength parameter defined as<sup>40</sup>

$$S = \left[ \frac{1}{3} \sum_{k=2,4,6} \frac{1}{2k+1} \left( (B_0^k)^2 + 2 \sum_{\substack{q \leq k \\ q > 0}} ((B_q^k)^2 + (B_q^k)^2) \right) \right]^{1/2} \quad (4)$$

has been also calculated to simplify the comparison of the crystal-field interaction in the different structures.

The obtained parameters and the energy level positions for each host and dopant ion are included in the Supporting Information. The energy level schemes obtained from these data has been used to analyze the optical spectra.

## ■ ASSOCIATED CONTENT

### Supporting Information

The Supporting Information is available free of charge at <https://pubs.acs.org/doi/10.1021/acsomega.9b02862>.

Crystal field parameters and crystal field strength values, calculated energy level positions for  $\text{Tb}^{3+}$  and  $\text{Yb}^{3+}$  ion in  $\text{InNbO}_4$ ,  $\text{InTaO}_4$ , and  $\text{InVO}_4$ , oxygen position and relative charge for oxygen ligands in In site used to obtain the crystal field parameters, graphical representations of the In local environment, and Miller indices,  $d$ -space, dispersion angle, and simulated X-ray diffraction intensity of  $\text{InVO}_4$ ,  $\text{InNbO}_4$ , and  $\text{InTaO}_4$  (PDF)

## ■ AUTHOR INFORMATION

### Corresponding Author

\*E-mail: [pablo.botella.vives@ltu.se](mailto:pablo.botella.vives@ltu.se).

### ORCID

Pablo Botella: 0000-0001-6930-8415

Alberto Vomiero: 0000-0003-2935-1165

Alka B. Garg: 0000-0003-4050-8469  
Francisco J. Manjón: 0000-0002-3926-1705  
Alfredo Segura: 0000-0002-9979-1302  
Daniel Errandonea: 0000-0003-0189-4221

### Author Contributions

The manuscript was written through contributions of all authors. All authors have given approval to the final version of the manuscript.

### Notes

The authors declare no competing financial interest.

## ACKNOWLEDGMENTS

The authors thank the financial support from the Spanish Ministerio de Ciencia, Innovación y Universidades, Spanish Research Agency (AEI), Generalitat Valenciana, and European Fund for Regional Development (ERDF, FEDER) under grants no. MAT2016-75586-C4-1/2-P, RTI2018-101020-B-I00, RED2018-102612-T (MALTA Consolier Team), and Prometeo/2018/123 (EFIMAT). P.B. acknowledges financial support from the Kempe Foundation and the Knut & Alice Wallenberg Foundation via a doctoral studentship. A.B.G. thanks the support provided by Universitat de Valencia to perform a research stay (Atracció de Talent, VLC-CAMPUS).

## REFERENCES

- Wang, Z. L. From nanogenerators to piezotronics—A decade-long study of ZnO nanostructures. *MRS Bull.* **2012**, *37*, 814.
- Li, Y.; Xu, S. The contribution of  $\text{Eu}^{3+}$  doping concentration on the modulation of morphology and luminescence properties of  $\text{InVO}_4:\text{Eu}^{3+}$ . *RSC Adv.* **2018**, *8*, 31905.
- Tang, A.; Ma, T.; Gu, L.; Zhao, Y.; Zhang, J.; Zhang, H.; Shao, F.; Zhang, H. Luminescence properties of novel red-emitting phosphor  $\text{InNb}_{1-x}\text{P}_x\text{O}_4:\text{Eu}^{3+}$  for white light emitting-diodes. *Mater. Sci.-Pol.* **2015**, *33*, 331–334.
- Ye, J.; Zou, Z.; Arakawa, H.; Oshikiri, M.; Shimoda, M.; Matsushita, A.; Shishido, T. Correlation of crystal and electronic structures with photophysical properties of water splitting photocatalysts  $\text{InMO}_4$  ( $M = \text{V}^{5+}, \text{Nb}^{5+}, \text{Ta}^{5+}$ ). *J. Photochem. Photobiol., A* **2002**, *148*, 79.
- Oshikiri, M.; Boero, M.; Ye, J.; Zou, Z.; Kido, G. Electronic structures of promising photocatalysts  $\text{InMO}_4$  ( $M = \text{V}, \text{Nb}, \text{Ta}$ ) and  $\text{BiVO}_4$  for water decomposition in the visible wavelength region. *J. Chem. Phys.* **2002**, *117*, 7313.
- Zou, Z.; Ye, J.; Arakawa, H. Structural properties of  $\text{InNbO}_4$  and  $\text{InTaO}_4$ : correlation with photocatalytic and photophysical properties. *Chem. Phys. Lett.* **2000**, *332*, 271.
- Balamurugan, C.; Vijayakumar, E.; Subramania, A. Synthesis and characterization of  $\text{InNbO}_4$  nanopowder for gas sensors. *Talanta* **2012**, *88*, 115–120.
- Chen, L.; Liu, Y.; Lu, Z.; Zeng, D. Shape-controlled synthesis and characterization of  $\text{InVO}_4$  particles. *J. Colloid Interface Sci.* **2006**, *295*, 440–444.
- Errandonea, D.; Popescu, C.; Garg, A. B.; Botella, P.; Martínez-García, D.; Pellicer-Porres, J.; Rodríguez-Hernández, P.; Muñoz, A.; Cuenca-Gotor, V.; Sans, J. A. Pressure-induced phase transition and band-gap collapse in the wide-band-gap semiconductor  $\text{InTaO}_4$ . *Phys. Rev. B* **2016**, *93*, No. 035204.
- Botella, P.; Errandonea, D.; Garg, A. B.; Rodríguez-Hernández, P.; Muñoz, A.; Achary, S. N.; Vomiero, A. High-pressure characterization of the optical and electronic properties of  $\text{InVO}_4$ ,  $\text{InNbO}_4$ , and  $\text{InTaO}_4$ . *SN Appl. Sci.* **2019**, *1*, 389.
- Garg, A. B.; Errandonea, D.; Popescu, C.; Martínez-García, D.; Pellicer-Porres, J.; Rodríguez-Hernández, P.; Muñoz, A.; Botella, P.; Cuenca-Gotor, V. P.; Sans, J. A. Pressure-Driven Isostructural Phase Transition in  $\text{InNbO}_4$ : In Situ Experimental and Theoretical Investigations. *Inorg. Chem.* **2017**, *56*, 5420.
- Errandonea, D.; Gomis, O.; García-Domene, B.; Pellicer-Porres, J.; Katari, V.; Achary, S. N.; Tyagi, A. K.; Popescu, C. New Polymorph of  $\text{InVO}_4$ : A High-Pressure Structure with Six-Coordinated Vanadium. *Inorg. Chem.* **2013**, *52*, 12790.
- Errandonea, D.; Tu, C.; Jia, G.; Martín, I. R.; Rodríguez-Mendoza, U. R.; Lahoz, F.; Torres, M. E.; Lavín, V. Effect of pressure on the luminescence properties of  $\text{Nd}^{3+}$  doped  $\text{SrWO}_4$  laser crystal. *J. Alloys Compd.* **2008**, *451*, 212–214.
- Muñoz-Santiuste, J. E.; Lavín, V.; Rodríguez-Mendoza, U. R.; Ferrer-Roca, C.; Errandonea, D.; Martínez-García, D.; Rodríguez-Hernández, P.; Muñoz, A.; Bettinelli, M. Experimental and theoretical study on the optical properties of  $\text{LaVO}_4$  crystals under pressure. *Phys. Chem. Chem. Phys.* **2018**, *20*, 27314.
- Yoo, S. H.; Kum, J. M.; Cho, S. O. Tuning the electronic band structure of PCBM by electron irradiation. *Nanoscale Res. Lett.* **2011**, *6*, 545.
- Tapasztó, L.; Dobrik, G.; Nemes-Incze, P.; Vertesy, G.; Lambin, P.; Biró, L. P. Tuning the electronic structure of graphene by ion irradiation. *Phys. Rev. B* **2008**, *78*, 233407.
- Shih, H.-R.; Liu, K.-T.; Teoh, L.-G.; Wei, L.-K.; Chang, Y.-S. Synthesis and photoluminescence properties of (La,Pr) co-doped  $\text{InVO}_4$  phosphor. *Microelectron. Eng.* **2015**, *148*, 10–13.
- Lu, M.; Li, Q.; Zhou, C.; Zhang, C.; Shi, H. Effects of nonmetal elements doping on the electronic structures of  $\text{InNbO}_4$ : first-principles calculations. *Mater. Res. Express* **2018**, *5*, No. 075505.
- Song, Y.; Sun, Z.; Wu, Y.; Chai, Z.; Wang, X. Investigation of the Preferential Doping Site and Regulating on the Visible Light Response and Redox Performance for Fe- and/or La Doped  $\text{InNbO}_4$ . *Inorg. Chem.* **2018**, *57*, 8558–8567.
- Rakesh, K.; Khaire, S.; Bhanke, D.; Dhanasekaran, P.; Deshpande, S. S.; Awate, S. V.; Gupta, N. M. Role of doping-induced photochemical and microstructural properties in the photocatalytic activity of  $\text{InVO}_4$  for splitting of water. *J. Mater. Sci.* **2011**, *46*, 5466–5476.
- Wetchakun, N.; Wanwaen, P.; Phanichphant, S.; Wetchakun, K. Influence of Cu doping on the visible-light-induced photocatalytic activity of  $\text{InVO}_4$ . *RSC Adv.* **2017**, *7*, 13911.
- Malingowski, A. C.; Stephens, P. W.; Huq, A.; Huang, Q.; Khalid, S.; Khalifah, P. G. Substitutional Mechanism of Ni into the Wide-Band-Gap Semiconductor  $\text{InTaO}_4$  and Its Implications for Water Splitting Activity in the Wolframite Structure Type. *Inorg. Chem.* **2012**, *51*, 6096–6103.
- Su, L.; Fan, X.; Cai, G.; Jin, Z. Tunable luminescence properties and energy transfer of  $\text{Tm}^{3+}$ ,  $\text{Dy}^{3+}$ , and  $\text{Eu}^{3+}$  co-activated  $\text{InNbO}_4$  phosphors for warm-white-lighting. *Ceram. Int.* **2016**, *42*, 15994–16006.
- Tang, A.; Zhang, D. F.; Yang, L. Synthesis and luminescence properties of novel red emitting phosphor  $\text{InNbO}_4:\text{Eu}^{3+}$  for white light emitting diodes. *Russ. Chem. Bull.* **2012**, *61*, 2172.
- Errandonea, D.; Ruiz-Fuertes, J. A. Brief review of the effects of pressure on wolframite-type oxides. *Crystals* **2018**, *8*, 71.
- Baran, E. J. Materials belonging to the  $\text{CrVO}_4$  structure type: preparation, crystal chemistry and physicochemical properties. *J. Mater. Sci.* **1998**, *33*, 2479.
- López-Moreno, S.; Rodríguez-Hernández, P.; Muñoz, A.; Errandonea, D. First-Principles Study of  $\text{InVO}_4$  under Pressure: Phase Transitions from  $\text{CrVO}_4$  to  $\text{AgMnO}_4$ -Type Structure. *Inorg. Chem.* **2017**, *56*, 2697–2711.
- Blasse, G.; Brill, A. Luminescence of Phosphors Based on Host Lattices  $\text{ABO}_4$  (A is Sc, In; B is P, V, Nb). *J. Chem. Phys.* **1969**, *50*, 2974.
- Tang, A.; Gu, L.; Shao, F.; Liu, X.; Zhao, Y.; Chen, H.; Zhang, H. Influence of  $\text{Bi}^{3+}$  content on photoluminescence of  $\text{InNbO}_4:\text{Eu}^{3+}$ ,  $\text{Bi}^{3+}$  for white light-emitting diodes. *Mater. Sci.-Pol.* **2017**, *35*, 435–439.
- Shia, Z.-R.; Chen, H.-L.; Tsai, Y.-Y.; Wu, S.; Chang, Y.-S. Synthesis and Photoluminescence Properties of  $\text{InVO}_4:\text{Eu}^{3+}$  Phos-

phors Prepared using Sol–Gel Method. *ECS Trans.* **2010**, *28*, 145–154.

(31) Brixner, L. H.; Chen, H.-Y. On the structural and luminescent properties of the  $\text{InTa}_{1-x}\text{Nb}_x\text{O}_4$  system. *Mater. Res. Bull.* **1980**, *15*, 607–612.

(32) Shen, J.; Yang, H.; Shen, Q.; You, Z. Synthesis and Characterization of  $\text{InVO}_4$  Nano-materials and their Photoluminescence Properties. *Procedia Eng.* **2014**, *94*, 64–70.

(33) Zeng, G.-S.; Yu, J.; Zhu, H.-Y.; Liu, H.-L.; Xing, Q.-J.; Bao, S.-K.; He, S.; Zou, J.-P.; Au, C.-T. Controllable synthesis of  $\text{InTaO}_4$  catalysts of different morphologies using a versatile sol precursor for photocatalytic evolution of  $\text{H}_2$ . *RSC Adv.* **2015**, *5*, 37603.

(34) Lacomba-Perales, R.; Ruiz-Fuertes, J.; Errandonea, D.; Martínez-García, D.; Segura, A. Optical absorption of divalent metal tungstates: Correlation between the band-gap energy and the cation ionic radius. *EPL (Eur. Lett.)* **2008**, *83*, 37002.

(35) Carnall, W. T.; Goodman, G. L.; Rajnak, K.; Rana, R. S. A systematic analysis of the spectra of the lanthanides doped into single crystal  $\text{LaF}_3$ . *J. Chem. Phys.* **1989**, *90*, 3443.

(36) Gruber, J. B.; Nash, K. L.; Yow, R. M.; Sardar, D. K.; Valiev, U. V.; Uzokov, A. A.; Burdick, G. W. Spectroscopic and magnetic susceptibility analyses of the  $^7\text{F}_1$  and  $^5\text{D}_4$  energy levels of  $\text{Tb}^{3+}(4f^8)$  in  $\text{TbAlO}_3$ . *J. Lumin.* **2008**, *128*, 1271–1284.

(37) Cascales, C.; Zaldo, C. Spectroscopic Characterization and Systematic Crystal-Field Modeling of Optically Active Rare Earth  $\text{RE}^{3+}$  Ions in the Bismuth Germanate  $\text{BiY}_{1-x}\text{R}_x\text{GeO}_5$  Host. *Chem. Mater.* **2006**, *18*, 3742–3753.

(38) Porcher, P.; Couto Dos Santos, M.; Malta, O. Relationship between phenomenological crystal field parameters and the crystal structure: The simple overlap model. *Phys. Chem. Chem. Phys.* **1999**, *1*, 397–405.

(39) Hernández-Rodríguez, M. A.; Muñoz-Santiuste, J. E.; Lavín, V.; Lozano-Gorrín, A. D.; Rodríguez-Hernández, P.; Muñoz, A.; Venkatramu, V.; Martín, I. R.; Rodríguez-Mendoza, U. R. High pressure luminescence of  $\text{Nd}^{3+}$  in  $\text{YAlO}_3$  perovskite nanocrystals. A crystal-field analysis. *J. Chem. Phys.* **2018**, *148*, No. 044201.

(40) Chang, N. C.; Gruber, J. B.; Leavitt, R. P.; Morrison, C. A. Optical spectra, energy levels, and crystal-field analysis of tripositive rare-earth ions in  $\text{Y}_2\text{O}_3$ . II. Kramers ions in  $\text{C}_2$  sites. *J. Chem. Phys.* **1982**, *76*, 3877.

(41) Gluba, M. A.; Nickel, N. H.; Karpensky, N. Interstitial zinc clusters in zinc oxide. *Phys. Rev. B* **2013**, *88*, 245201.

(42) Mondal, S.; Appalakondaiah, S.; Vaitheeswaran, G. High pressure structural, electronic, and optical properties of polymorphic  $\text{InVO}_4$  phases. *J. Appl. Phys.* **2016**, *119*, No. 085702.

(43) Zhou, J.; Huang, F.; Xu, J.; Chen, H.; Wang, Y. Luminescence study of a self-activated and rare earth activated  $\text{Sr}_3\text{La}(\text{VO}_4)$ . *J. Mater. Chem. C* **2015**, *3*, 3023–3028.

(44) Ronde, H.; Blasse, G. The nature of the electronic transitions of the vanadate group. *J. Inorg. Nucl. Chem.* **1978**, *40*, 215–219.

(45) Nakajima, T.; Isobe, M.; Tsuchiya, T.; Ueda, Y.; Manabe, T. Correlation between Luminescence Quantum Efficiency and Structural Properties of Vanadate Phosphors with Chained, Dimerized, and Isolated  $\text{VO}_4$  Tetrahedra. *J. Phys. Chem. C* **2010**, *114*, 5160–5167.

(46) Van de Krol, R.; Ségolini, J.; Enache, C. S. Influence of point defects on the performance of  $\text{InVO}_4$  photoanodes. *J. Photonics Energy* **2011**, *1*, No. 016001.

(47) Nakajima, T.; Isobe, M.; Tsuchiya, T.; Ueda, Y.; Manabe, T. Photoluminescence property of vanadates  $\text{M}_2\text{V}_2\text{O}_7$  (M: Ba, Sr and Ca). *Opt. Mater.* **2010**, *32*, 1618–1621.

(48) Delosh, R. G.; Tien, T. Y.; Gibbons, E. F.; Zacmanidis, P. J.; Stadler, H. L. Strong Quenching of  $\text{Tb}^{3+}$  Emission by  $\text{Tb}-\text{V}$  Interaction in  $\text{YPO}_4-\text{YVO}_4$ . *J. Chem. Phys.* **1970**, *53*, 681.

(49) Blasse, G.; Brill, A. Investigations of  $\text{Tb}^{3+}$ -activated phosphors. *Philips Res. Rep.* **1967**, *22*, 481–504.

(50) Huignard, A.; Gacoin, T.; Boilot, J.-P. Synthesis and Luminescence Properties of Colloidal  $\text{YVO}_4:\text{Eu}$  Phosphors. *Chem. Mater.* **2000**, *12*, 1090–1094. Wei, X.; Huang, S.; Chen, Y.; Guo, C.; Yin, M.; Xu, W. Energy transfer mechanisms in  $\text{Yb}^{3+}$  doped  $\text{YVO}_4$

near-infrared downconversion phosphor. *J. Appl. Phys.* **2010**, *107*, 103107.

(51) Li, G. L.; Yin, Z. Theoretical insight into the electronic, optical and photocatalytic properties of  $\text{InMO}_4$  (M = V, Nb, Ta) photocatalysts. *Phys. Chem. Chem. Phys.* **2011**, *13*, 2824–2833.

(52) Feng, H.; Hou, D.; Huang, Y.; Hu, X. Facile synthesis of porous  $\text{InNbO}_4$  nanofibers by electrospinning and their enhanced visible-light-driven photocatalytic properties. *J. Alloys Compd.* **2014**, *592*, 301–305.

(53) Back, M.; Massari, A.; Boffelli, M.; Gonella, F.; Riello, P.; Cristofori, D.; Riccò, R.; Enrichi, F. Optical investigation of  $\text{Tb}^{3+}$ -doped  $\text{Y}_2\text{O}_3$  nanocrystals prepared by Pechini-type sol–gel process. *J. Nanopart. Res.* **2012**, *14*, 792.

(54) Muenchausen, R. E.; Jacobsohn, L. G.; Bennett, B. L.; McKigney, E. A.; Smith, J. F.; Valdez, J. A.; Cooke, D. W. Effects of Tb doping on the photoluminescence of  $\text{Y}_2\text{O}_3:\text{Tb}$  nanophosphors. *J. Lumin.* **2007**, *126*, 838–842.

(55) Flores-Gonzalez, M. A.; Ledoux, G.; Roux, S.; Lebbou, K.; Perriat, P.; Tillement, O. Preparing nanometer scaled Tb-doped  $\text{Y}_2\text{O}_3$  luminescent powders by the polyol method. *J. Solid State Chem.* **2005**, *178*, 989–997.

(56) Meng, Q.; Chen, B.; Xu, W.; Yang, Y.; Zhao, X.; Di, W.; Lu, S.; Wang, X.; Sun, J.; Cheng, L.; Yu, T.; Peng, Y. Size-dependent excitation spectra and energy transfer in  $\text{Tb}^{3+}$ -doped  $\text{Y}_2\text{O}_3$  nanocrystalline. *J. Appl. Phys.* **2007**, *102*, 093505–093501.

(57) Pavitra, E.; Raju, G. S. R.; Ko, Y. H.; Yu, J. S. A novel strategy for controllable emissions from  $\text{Eu}^{3+}$  or  $\text{Sm}^{3+}$  ions co-doped  $\text{SrY}_2\text{O}_4:\text{Tb}^{3+}$  phosphors. *Phys. Chem. Chem. Phys.* **2012**, *14*, 11296–11307.

(58) Chukova, O.; Nedilko, S.; Titov, Y.; Sheludko, V. Crystallographic Features and Nature of Luminescence Centres of the Niobate and Tantalate Compounds with Layered Perovskite-Like Structure. *Open Mater. Sci. J.* **2018**, *12*, 2–13.

(59) Van Pieterse, L.; Heeroma, M.; de Heer, E.; Meijerink, A. Charge transfer luminescence of  $\text{Yb}^{3+}$ . *J. Lumin.* **2000**, *91*, 177–193.

(60) Boulon, G. Why so deep research on  $\text{Yb}^{3+}$ -doped optical inorganic materials? *J. Alloys Compd.* **2008**, *451*, 1–11.

(61) Kuboniwa, S.; Hoshina, T. Luminescent Properties of  $\text{Tb}^{3+}$  in Oxygen-Dominated Compounds. *J. Phys. Soc. Jpn.* **1972**, *32*, 1059–1068.

(62) Henderson, B.; Imbusch, G. F. *Optical spectroscopy of inorganic solids*; 1st ed., Academic press: Oxford: New York, 1989; pp 388–403.

(63) Anisimov, V. A.; Dmitryuk, A. V.; Karapetyan, G. O. Kinetic study of  $\text{Tb}^{3+}(^5\text{D}_3)$  luminescence in phosphate glasses. *J. Appl. Spectrosc.* **1985**, *43*, 747.

(64) May, P. S.; Sommer, K. D.  $\text{Tb}^{3+}$  Luminescence in Tb-Doped and Tb/Gd-Doped  $\text{CsCdBr}_3$  Crystals:  $^5\text{D}_4 \rightarrow ^5\text{D}_3$  Cross-Relaxation Rates in  $\text{Tb}^{3+}$  Pair. *J. Phys. Chem. A* **1997**, *101*, 9571.

(65) Sharma, K. G.; Singh, N. Re-dispersible  $\text{CaWO}_4:\text{Tb}^{3+}$  nanoparticles: Synthesis, characterization and photoluminescence studies. *J. Lumin.* **2013**, *139*, 98–103.

(66) Sayer, M. Luminescence in the Alkali Metavanadates. *Phys. Status Solidi (a)* **1970**, *1*, 269.

(67) Laversenne, L.; Guyot, Y.; Goutaudier, C.; Cohen-Adad, M. T.; Boulon, G. Optimization of spectroscopic properties of  $\text{Yb}^{3+}$ -doped refractory sesquioxides: cubic  $\text{Y}_2\text{O}_3$ ,  $\text{Lu}_2\text{O}_3$  and monoclinic  $\text{Gd}_2\text{O}_3$ . *Opt. Mater.* **2001**, *16*, 475–483.

(68) Bharat, L. K.; Jeon, S. K.; Krishna, K. G.; Yu, J. S. Rare-earth free self-luminescent  $\text{Ca}_2\text{KZn}_2(\text{VO}_4)_3$  phosphors for intense white light-emitting diodes. *Sci. Rep.* **2017**, *7*, 42348.

(69) Boutinaud, P.; Cavalli, E.; Bettinelli, M. Emission quenching induced by intervalence charge transfer in  $\text{Pr}^{3+}$ - or  $\text{Tb}^{3+}$ -doped  $\text{YNbO}_4$  and  $\text{CaNb}_2\text{O}_6$ . *J. Phys.: Condens. Matter* **2007**, *19*, 386230.